# Numerical Investigation of Self-Heating Effects of Oxide-Confined Vertical-Cavity Surface-Emitting Lasers

Yang Liu, *Member, IEEE*, Wei-Choon Ng, *Member, IEEE*, Kent D. Choquette, *Fellow, IEEE*, and Karl Hess, *Fellow, IEEE*

***Abstract*—We present a comprehensive numerical model to simulate self-heating effects of oxide-confined vertical-cavity surface-emitting lasers (VCSELs) under continuous-wave operation. The model self-consistently accounts for the close interaction between optical, electrical, and thermal processes in VCSELs. In particular, hot carriers and nonequilibrium optical phonons in the quantum wells are modeled by solving a carrier energy balance equation and an optical phonon rate equation. Our numerical simulations reveal that they are responsible for aggravated thermal rollovers in VCSELs' *L–I* characteristics. Detailed comparisons are made and good agreement is obtained between simulations and experiments for the *L–I–V* and lasing wavelength characteristics of VCSELs with varying oxide aperture size. Various mechanisms that result in the *L–I* thermal rollover behavior are also investigated with the aid of simulations.**

***Index Terms*—Charge carrier processes, distributed Bragg reflector lasers, hot carriers, laser reliability, laser thermal factors, semiconductor heterojunctions, semiconductor lasers.**

## I. Introduction

VERTICAL-CAVITY surface-emitting lasers (VCSELs) have recently been a subject of intensive research efforts due to their important role in high-speed, densely integrated optoelectronics. In practice, the maximum continuous-wave (CW) output power of VCSELs is limited by self-heating effects, and the output power saturates and even decreases at high injection level. This is the commonly observed premature "thermal rollover" of the CW light output power in VCSELs. In the early work of Hasnain *et al.* [1], the causes of the thermal rollover have been qualitatively analyzed by considering the temperature dependence of optical gain, lasing mode, and effective threshold current based on a phenomenological approach. In brief, the thermal rollover behavior is caused by the positive feedback process between raised temperature and reduced power conversion efficiency. In state-of-the-art VCSEL designs, oxide apertures are introduced to achieve better confinements of both current injections and optical modes [2]–[4], and the scalability of such devices has been investigated with respect to threshold current and intrinsic threshold voltage [5]. In VCSELs with small oxide apertures, the self-heating problem becomes more severe due to several factors: the enhanced power density in small device volume, severe Joule heating in distributed Bragg reflector (DBR) stacks, and the oxides that act as electrical and thermal blocking layers. In this work, we quantitatively investigate the aggravated self-heating problem in oxide-confined VCSELs. For such a purpose, it is necessary to develop a self- consistent VCSEL model accounting for the electrical, optical, and thermal characteristics and their close interaction.

There has been a lot of on-going effort on the thermal modeling of both edge-emitting laser diodes and VCSELs with different levels of incorporated physics and self-consistency [6]–[16]. In the early work of Nakwaski and Osinski [6], the thermal properties of VCSELs under threshold condition were numerically investigated. A review of the numerical modeling of VCSELs thermal properties was later presented in [7]. In the work of Scott *et al.* on VCSEL's temperature effects [8], a two dimensional carrier transport simulator has been developed without a thermal diffusion model, and the junction temperature was obtained phenomenologically. Yu *et al.* developed a numerically appealing rate equation approach with an oversimplified carrier transport treatment and an empirical temperature dependence of the threshold current density [9], [10]. The comprehensive hydrodynamic model by Winston and Hayes [11] treats the DBR structures in detail, but only in one dimension. Device-level simulations have been performed to investigate the self-heating effects for both VCSELs and long wavelength edge emitting lasers by Piprek *et al.* [12]–[14]. However, the impact of oxide aperture in VCSELs was not addressed. In a recent work of Streiff *et al.* [15], a coupled electro-opto-thermal VCSEL simulation model was developed, but the simulation results presented was only for moderate injection level below the thermal rollover condition. One of the most comprehensive numerical models accounts for two-dimensional (2-D) current and heat transport, transverse mode competition, and thermal lensing for both gain-guided and index-guided structures [16]. However, the modeling of hot carriers and nonequilibrium optical phonons was lacking.

The VCSEL thermal modeling works mentioned so far have not considered the additional self-heating due to hot quantum-

Manuscript received August 23, 2004; revised September 28, 2004. The work of K. Hess and Y. Liu was supported in part by the Office of Naval Research under Grant N00014-98-1-0604.

Y. Liu is with the Department of Electrical and Computer Engineering, University of Illinois at Urbana-Champaign, Urbana, IL 61801 USA and also with the Integrated Circuits Laboratory, Stanford University, Stanford, CA 94305 USA (e-mail: yangliu@gloworm.stanford.edu).

W.-C. Ng was with the Department of Electrical and Computer Engineering, University of Illinois at Urbana-Champaign, Urbana, IL 61801 USA. He is now with Integrated Systems Engineering, Inc., San Jose, CA 95113 USA.

K. D. Choquette and K. Hess are with the Department of Electrical and Computer Engineering, University of Illinois at Urbana-Champaign, Urbana, IL 61801 USA.

Digital Object Identifier 10.1109/JQE.2004.839239

well (QW) carriers and nonequilibrium optical phonons. It has long been found that hot carriers can directly influence the temperature dependence of laser diode threshold [17]. It has also been well established, both theoretically and experimentally, that the temperature of QW carriers and optical phonons in laser diodes can be significantly above that of acoustic phonons due to a finite optical phonon decay rate [18]–[23]. The resultant impact on laser diode performance has been extensively investigated with respect to gain saturation [24], transverse mode behavior [25], and modulation response [26]–[29]. The $L$–$I$ thermal rollover caused by hot carriers and hot phonons was demonstrated in [30] based on a simple rate equation analysis, where the acoustic phonons were treated as a thermal bath. In order to model the plasma-heating induced nonlinear gain, Ning and Moloney derived a set of rate equations based on a microscopic laser theory [31], and later applied it to examine the self-heating problem of VCSELs [32]. Some of their theoretical predictions were in qualitative agreement with experiments, but the lack of 2-D current and heat transport modeling makes their approach insufficient for a quantitative simulation.

In this work, we present numerical investigations based on a comprehensive laser diode simulator, MINILASE [28]. It has recently been extended to simulate VCSEL structures [33], [34], particularly on VCSELs' modulation responses [35] and electrical turn-on characteristics [36]. A thermal diffusion equation based on energy balance has also been incorporated into MINILASE to solve the lattice (acoustic phonon) temperature distribution over the entire device [37]. Hot carriers and nonequilibrium optical phonons have been previously modeled in MINILASE to study the modulation response of edge emitting laser diodes [28]. However, the carrier temperature was obtained by requiring that total carrier energy loss due to carrier-carrier scattering is zero. In this work, a new and more complete model based on energy balance is incorporated into MINILASE to solve the carrier and optical phonon temperatures in the QWs. This model is self-consistently coupled with the acoustic phonon temperature model as well as the electrical and optical models in the simulator. The impact of hot carriers and nonequilibrium optical phonons is demonstrated with the extended simulation capabilities. Detailed correlations between simulations and experimental measurements are conducted for VCSELs with varying oxide aperture sizes. Excellent agreement is obtained for the VCSELs' lasing wavelength, voltage, and light output power as functions of the current bias. The self-heating problem is observed both experimentally and numerically to be more severe for VCSELs with small oxide aperture size. In the last part, we discuss the underlying causes of the thermal rollover behavior in detail.

## II. Simulation Models

The MINILASE simulator has three tightly coupled components to self-consistently address the electronic, optical, and thermal processes. Detailed descriptions on MINILASE have been given in previous work [28], [33], [34]. In this section, we will highlight the key features and elaborate on the extended capabilities of hot carrier and nonequilibrium optical phonon modeling.

### A. Electronic Model

The physics-based carrier transport model of MINILASE is applicable to oxide confined VCSEL structures. A typical oxide-confined structure is illustrated in Fig. 1(a). Fig. 1(b) is a schematic plot of the simulation domain for the electronic solver, and cylindrical symmetry is assumed. A set of semiconductor equations, including Poisson and continuity (for both electrons and holes) equations, are solved to obtain the distribution of the electrostatic potential and electron–hole quasi-Fermi levels over the entire simulation domain. The carrier transport at heterojunctions is modeled by thermionic emission [38]. Due to the primary importance of QWs in laser diodes, a careful treatment of QW carriers is necessary. An $8 \times 8$ k.p band-structure solver has been incorporated to calculate the density of states and optical matrix elements of 980-nm InGaAs–GaAs QWs [39]. The QW carriers are divided into two ensembles with distinct quasi-Fermi levels: continuum carriers for those with energy above the QW barrier, and bound carriers otherwise [28]. Both carrier–carrier and carrier–optical phonon interactions are accounted for to model the carrier capture from the continuum states to the bound states and intrasubband scattering. The equations describing such important processes have been obtained by considering Fermi–Dirac (for carriers) and Bose-Einstein (for phonons) statistics and detailed balance, in the framework of Fermi's golden rule [28, eq. (10), (11)].

Among various recombination processes, the Shockley–Read–Hall (SRH) process is caused by recombination/generation involving deep-level impurities, and its rate is given by [38]

$$U_{\mathrm{SRH}} = \frac{n \cdot p - n_i^2}{\tau_n(n + n_1) + \tau_p(p + p_1)} \tag{1}$$

where $n, p$ are electron and hole concentrations, $n_i$ is the intrinsic carrier concentration, $\tau_{n,p}$ are SRH recombination lifetimes for electron–hole, and $n_1/p_1$ are electron–hole concentration when the quasi-Fermi level is positioned at the trap energy level. We model the Auger recombination rate as [40]

$$U_{\mathrm{Aug}} = C_n \cdot n^2 \cdot p + C_p \cdot n \cdot p^2. \tag{2}$$

The Auger coefficients $C_{n,p}$ account for processes where the second electron–hole gains the energy, respectively. Usually, $C_n$ is much smaller than $C_p$. The spontaneous emission rate in the bulk region is given by $U_{\mathrm{spon}} = B_{\mathrm{spon}} \cdot n \cdot p$, where $B_{\mathrm{spon}}$ is the bimolecular recombination coefficient. In the QWs, the spontaneous and stimulated recombinations are accurately modeled based on the density of states and optical matrix elements computed from the k.p solver and Fermi–Dirac statistics. The DBR stacks as shown in Fig. 1(a) play a very important role in the thermal properties of VCSELs, because they are responsible for a large fraction of the total voltage drop across the device. To model the detailed structure of several tens of alternating AlGaAs–GaAs pairs will increase the computation volume significantly, and render 2-D simulations unfeasible. A more practical approach is to model the top and bottom DBR stacks as two regions composed of bulk semiconductors with effective mobilities. This is because the high doping concentration ($> 10^{18}\mathrm{cm}^{-3}$) in the DBR stacks results in high carrier-carrier and carrier-impurity scattering rates, which make

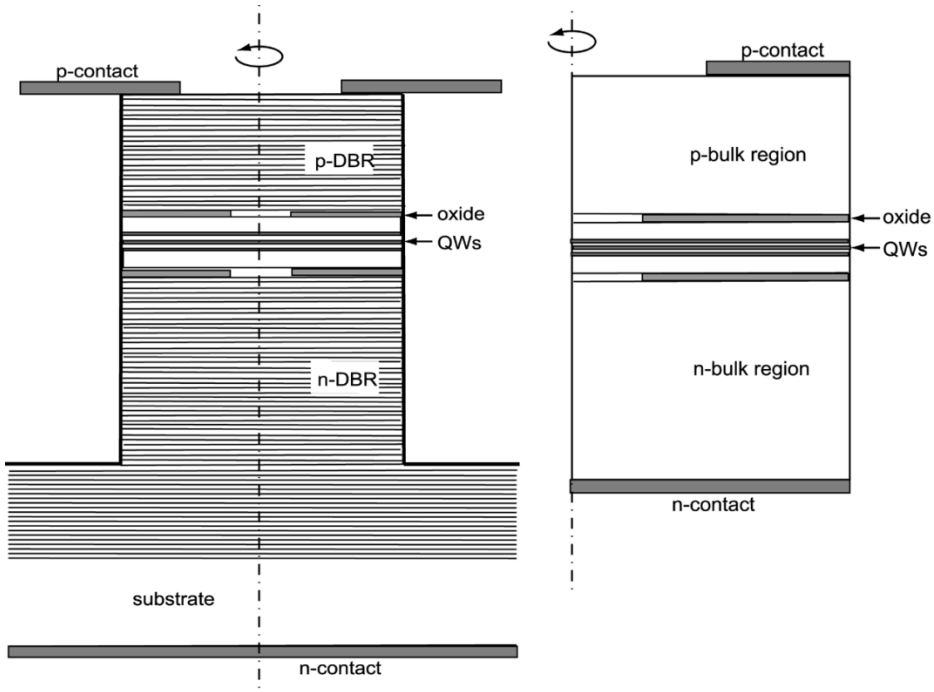


Fig. 1. (a) Schematic cross-sectional plot of a typical double oxide-confined VCSEL device. (b) Simulation domain of the electronic model for the device in (a).

the actual details of the DBR band diagram less important in modeling the carrier transport. In our work, we adopt this approach, as illustrated in Fig. 1(b). The carrier mobilities in the bulk regions are adjusted so that the total $I$–$V$ characteristics above the threshold match the experimental results. Nevertheless, the following problem has to be addressed to model the minority carrier recombination correctly: what bandgap value should be used for the replacement bulk material in the simulation? The real DBR pairs are composed of AlGaAs and GaAs, which have significant bandgap difference. The narrow bandgap GaAs layers tend to cause accumulations of the minority carriers, which leads to significant recombination current at high forward bias due to both SRH and spontaneous recombination processes. Since the minority carrier concentration is exponentially dependent on the bandgap, we simulate the DBR stacks as AlGaAs bulk region with low Al mole fraction to avoid underestimations of the leakage current.

### *B. Optical Model*

There have been various VCSEL optical models presented in the literature, and a comprehensive benchmark was given in [41]. In this work, a self-consistent effective index solver is used [42]. The scalar optical solver is fast and ideal for tight coupling with the electronic and thermal models. The simulation domain of the optical solver includes all the alternating DBR layers with high/low refractive indices, $n_{\rm rh}/n_{\rm rl}$. The effective index solver is capable of accurately calculating the resonant frequency and modal profile of oxide confined structures. The temperature dependence of refractive indices is accounted for by self-consistent coupling with the thermal model.

The photon number in the resonant cavity is determined by a photon number rate equation, which balances the modal loss, modal gain, and spontaneous emission coupled into the resonant mode. The accurate modeling of the optical modal loss, or equivalently the threshold gain, is generally difficult for oxide-confined structures. As discussed in [41], various vectorial models can produce significantly different threshold gain values. In general, the total optical modal loss can be expressed as $1/\tau_{\rm ph} = L_{\rm mirror} + L_{\rm scatt} + L_{\rm abs}$, where $\tau_{\rm ph}$ is the photon lifetime, and $L_{\rm mirror}$ is the loss due to the DBR mirrors. $L_{\rm scatt}$ is the loss due to aperture scattering [43], refractive index fluctuation of the alloys [44], and surface roughness [45]. $L_{\rm abs}$ is due to free carrier [46] and intervalence band [47] absorptions. The optical efficiency, as defined by the ratio of photons collected by the detector and total emitted photons, is given by $L_{\rm mirror}/(1/\tau_{\rm ph})$. In this work, the mirror loss is assumed to be independent of the oxide aperture size. $L_{\rm scatt}$ is tuned as a fitting parameter for devices with different aperture sizes to match both the threshold current and the initial slope efficiency of the measured light-current curves. The absorption loss $L_{\rm abs}$ is modeled as $L_{\rm abs} = (c/n_r)|\Phi|^2(k_n n + k_p p)$, where $|\Phi|^2$ is the normalized local field intensity, $c$ is the speed of light, $n_r$ is the refractive index, and $k_n$ and $k_p$ are coefficients accounting for both free carrier and intervalence band absorptions.

We only consider single-mode operation in our simulations. This is a simplification of the realistic VCSEL operation. At low bias, small oxide apertures confine the lateral current spreading and favor the selection of the fundamental mode. However, as the device temperature increases at higher biases, the modal gain peak shifts to the higher energy end, and therefore enhances the competition of higher order modes. Nevertheless, the single-mode assumption is still reasonable, since different lasing modes consume the same QW carrier ensemble and the main quantity of our interest is the overall output power.

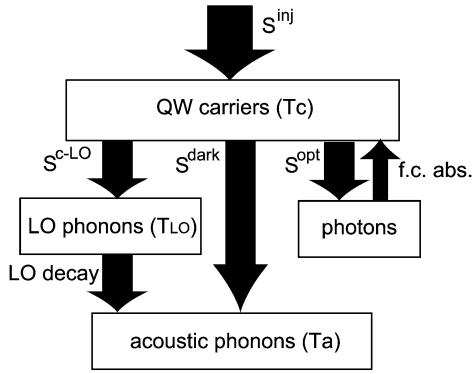


Fig. 2. Energy flow diagram between QW carrier, optical phonon, acoustic phonon, and photon systems.

### C. Thermal Model

We model the lattice (acoustic phonon) temperature over the entire device, and the carrier and optical phonon temperature only for the QWs. A detailed description of the lattice thermal model has been presented in [37]. Basically, the thermal diffusion equation for the lattice temperature $T_l$ is given by $\nabla \cdot \kappa_{\rm latt} \nabla T_l = \nabla \cdot (\vec{w}_n - \vec{w}_p) - Q'$, where $\kappa_{\rm latt}$ is the lattice thermal conductivity. $\vec{w}_n$ and $\vec{w}_p$ are energy fluxes carried by the electrons and holes, respectively. Their divergence accounts for the Joule heat, Thomson heat and Peltier heat. $Q'$ includes the heat source due to SRH recombination. An improvement in this work is the inclusion of a heat source due to the reabsorption of photons in $Q'$. A Dirichlet thermal boundary condition is used at the top annular and bottom contacts with a contact thermal resistance of $\sigma_{\rm thermal}$. At all other surfaces, the heat transfer to the air is assumed to be small, and a Neumann boundary condition is therefore used.

The QW carrier and optical phonon temperature model is based on energy balance. The interaction of energy fluxes in the QWs is illustrated in Fig. 2. An energy balance equation is solved for each of the carrier and optical phonon systems. The QW electrons and holes are assumed to have equal temperature $T_c$. This implies that electrons and holes are allowed to exchange energy rapidly, as confirmed by Monte Carlo simulations [48]. The energy balance equation for QW carriers is given by

$$\frac{\partial(E_{\rm el}+E_{\rm hl})}{\partial t} = S^{\rm inj} + S^{\rm opt} + S^{\rm abs} + S^{c-{\rm LO}} + S^{\rm dark} + \nabla \cdot \vec{S}^{\rm dd} + (\vec{j}_p \cdot \nabla E_v - \vec{j}_n \cdot \nabla E_c). \quad (3)$$

$E_{\rm el}$ and $E_{\rm hl}$ are the total energies of the electrons and holes, respectively, accounting for both the continuum and bound states. The time derivative on the left reduces to zero at steady state. The net energy flux due to current injection and leakage is given by

$$S^{\rm inj} = \frac{(E_c^b + E_g/2)}{d}\left(j_{\rm el}^{\rm major} - j_{\rm el}^{\rm minor}\right) + \frac{(E_v^b + E_g/2)}{d}\left(j_{\rm hl}^{\rm major} - j_{\rm hl}^{\rm minor}\right) \quad (4)$$

where $d$ is the QW thickness, and $E_c^b$ and $E_v^b$ are the conduction and valence band QW depth, respectively. $E_g$ is the QW bandgap, and we choose the middle of the bandgap as the energy reference point. $j_{\rm el}^{\rm major}, j_{\rm el}^{\rm minor}, j_{\rm hl}^{\rm major}$, and $j_{\rm hl}^{\rm minor}$ are the thermionic majority and minority carrier fluxes for electrons and holes, respectively. The energy flux associated with the spontaneous and stimulated recombinations transfers energy from the carriers to the photons. It is given by

$$S^{\rm opt} = -c/n_r \cdot g(\omega_c) \cdot \tilde{S} \cdot \hbar\omega_c - \int Z(\omega) \cdot r^{\rm spon}(\omega) \cdot \hbar\omega \cdot d\omega \quad (5)$$

where $\omega_c$ is the lasing frequency, and $\tilde{S}$ is the local photon density, taken as a product of the total photon number and the field pattern, $|\Phi|^2$. $g(\omega), Z(\omega)$, and $r^{\rm spon}(\omega)$ are the material gain, local photon density of states, and broadened spontaneous emission spectrum, respectively. Their exact definitions and calculations have been presented in [28]. We note that the carriers are injected from the top of the QWs, but optically recombine mostly at the bottom of the QWs. This energy difference leads to the heating of the carrier and optical phonon systems. The reabsorption of photons due to intervalence band and free carrier absorptions is an additional source of heating modeled by $S^{\rm abs} = L_{\rm abs} \cdot \tilde{S} \cdot \hbar\omega_c$. Energy can be rapidly transferred from the QW carriers to the longitudinal-optical (LO) phonons through efficient carrier-LO phonon scattering. The associated energy flux is given by $S^{c-{\rm LO}} = -\hbar\omega_{\rm LO}(U^{{\rm el}-{\rm LO}} + U^{{\rm hl}-{\rm LO}})$, where $\hbar\omega_{\rm LO}$ is the LO phonon energy, and $U^{{\rm el}-{\rm LO}}$ and $U^{{\rm hl}-{\rm LO}}$ are LO phonon scattering rates with electrons and holes, respectively. The electron-LO phonon scattering rate accounts for both the capture process and the intrasubband scattering as follows [28]:

$$U^{{\rm el}-{\rm LO}} = \sum_{i',i} \int_{E_{i'}}^{\infty} dE' \rho^{i'}(E') \times \int_{E_i}^{\infty} dE \rho^i s^{{\rm el}-{\rm LO}}(E', E) \cdot \delta(E' - E - \hbar\omega_{\rm LO}) \cdot [f'(1-f)(n_q+1) - (1-f')f n_q] \quad (6)$$

where the summations are over all subbands, $i$ and $i'$, and the integrals are from the subband edges, $E_i$ and $E_{i'}$, to infinity including the continuum states. The Dirac function in this expression is for energy conservation. We have a similar expression for $U^{{\rm hl}-{\rm LO}}$. The density of states of the initial and final carrier states, $\rho^{i'}$ and $\rho^i$, are obtained from the k.p solver. $s^{{\rm el}-{\rm LO}}$ is the microscopic scattering probability, which is an input parameter in the simulations. The initial and final state occupation probabilities, $f'$ and $f$, obey the Fermi–Dirac statistics with a carrier temperature $T_c$. The LO phonon occupation number $n_q$ is assumed to follow the Bose–Einstein statistics as

$$n_q = \frac{1}{\exp\left(\frac{\hbar\omega_{\rm LO}}{k_B T_{\rm LO}}\right) - 1} \quad (7)$$

where $k_B$ is the Boltzmann constant and $T_{\rm LO}$ is the LO phonon temperature. It can be seen in (6) that the scattering rate becomes zero for $T_c = T_{\rm LO}$, as it should be from the requirement of detailed balance. In general, we have $T_c > T_{\rm LO}$, but the difference is usually small because of the large carrier-phonon scattering probability. $S^{\rm dark}$ is the heat flux due to dark recombination, which includes both the Auger and SRH processes. We do not

consider the phonon assisted Auger process in this work. For the Auger processes considered, there is energy equal to the QW bandgap that contributes to the QW carrier energy. For the SRH process, it is difficult to determine the contributions from carriers at different energy levels. Therefore, we simply take an average value. $S^{\mathrm{dark}}$ is thereby expressed as

$$S^{\mathrm{dark}} = -2\bar{\varepsilon}_c U_{\mathrm{SRH}} + E_g U_{\mathrm{Aug}} \tag{8}$$

where $\bar{\varepsilon}_c = (E_{\mathrm{el}} + E_{\mathrm{hl}})/(n+p)$ is the average QW carrier energy, and the prefactor of two accounts for the fact that each SRH process eliminates an electron–hole pair. The energy flux associated with the lateral drift-diffusion of QW carriers is given by

$$\vec{S}^{\mathrm{dd}} = C_e k_B T_c \left( -\vec{j}_n - \vec{j}_p + nD_n \frac{\nabla T_c}{T_c} + pD_p \frac{\nabla T_c}{T_c} \right) \tag{9}$$

where $\vec{j}_n$ and $\vec{j}_p$ are lateral drift-diffusion fluxes, and $D_n$ and $D_p$ are diffusion coefficients for electrons and holes, respectively. $C_e$ is the energy flow factor, as introduced in [49]. The last term in (3) represents the electron and hole Joule heat associated with the lateral drift-diffusion within the QWs.

A phonon rate equation is obtained for the LO phonon ensemble based on energy balance. As shown in Fig. 2, the energy gain of the LO phonons is from carrier-LO phonon scattering, and the energy loss is due to the decay of the LO phonons into acoustic phonons. Therefore, the phonon rate equation is written as [28]

$$\frac{1}{2\pi^2}\int_0^{\vec{Q}_{\max}} d\vec{Q}\cdot\vec{Q}\int_{-q_{z0}}^{q_{z0}} dq_z \frac{\partial n_{\vec{q}}}{\partial t} = -\frac{S^{c-\mathrm{LO}}}{\hbar\omega_{\mathrm{LO}}} - \frac{1}{2\pi^2}\int_0^{\vec{Q}_{\max}} d\vec{Q}\cdot\vec{Q}\int_{-q_{z0}}^{q_{z0}} dq_z \frac{n_{\vec{q}} - n^0_{\vec{q}}}{\tau_{\mathrm{LO}}} \tag{10}$$

where the integrating variable $\vec{q} = (\vec{Q}, q_z)$ is the momentum vector of the 2-D, nonequilibrium LO phonons in the QWs, the ranges of which are $[0, \vec{Q}_{\max}]$ and $[-q_{z0}, q_{z0}]$, respectively. The term on the left-hand side of the equation is the net generation rate of the LO phonons, which becomes zero at steady state. The first term on the right is the LO phonon generation rate due to carrier-phonon scattering, where $-S^{c-\mathrm{LO}}$ is the energy flux contributing to the LO phonons, and $\hbar\omega_{\mathrm{LO}}$ is the LO phonon energy. The second term on the right gives the rate of the LO phonon decay into acoustic phonons. $n_{\vec{q}}$ is the nonequilibrium LO phonon occupation number and is related to $T_{\mathrm{LO}}$ by (7). $n^0_{\vec{q}}$ is the equilibrium occupation number at $T_{\mathrm{LO}} = T_l$. $\tau_{\mathrm{LO}}$ is the characteristic time of the LO phonon decay process. The LO phonon decay is usually of the order of a few picoseconds, and is a slow process as compared to the sub-picosecond carrier-LO phonon scattering. Therefore, this "phonon bottleneck" effect heats up the LO phonons, which in turn elevates the QW carrier temperature.

### *D. Self-Consistent Coupling of Models*

The complete simulation flowchart is given in Fig. 3. For a steady state simulation, the k.p and optical solvers are called first to compute the QW bandstructure and the optical-mode information. The set of nonlinear electronic transport equations, including the Poisson, continuity, photon rate, QW carrier energy balance, and phonon rate equations, are solved using the Newton method. If the Newton method does not converge in the first iteration, we assert that full convergence is not achieved. The thermal diffusion equation is then solved. Based on the updated lattice temperature profile, a recomputation is conducted for temperature-dependent material parameters including the bandgap, carrier mobilities, and refractive indices. We use Varshni formula for the temperature dependence of the energy bandgap

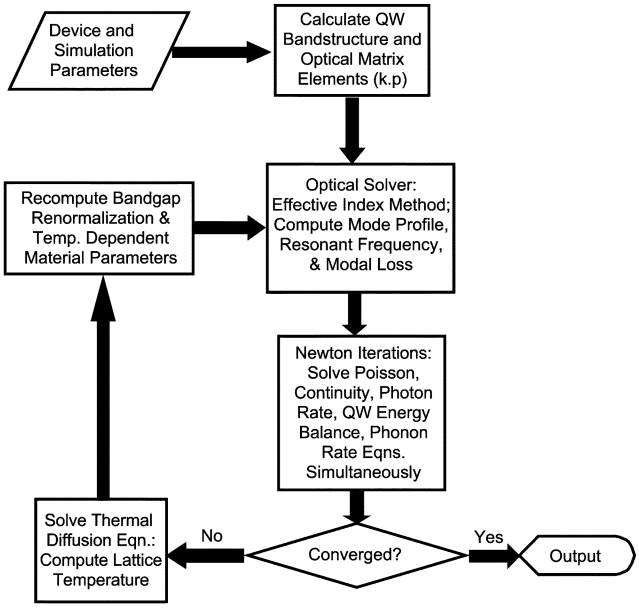


Fig. 3. Flowchart of the self-consistently coupled simulation in MINILASE.

$$E_g(T_l) = E_g(T_l = 300K) + \frac{A_g T_l^2}{T_l + B_g} - \frac{A_g \cdot 300^2}{300 + B_g} \tag{11}$$

where $A_g$ and $B_g$ are temperature coefficients. The temperature dependence of the carrier mobilities is assumed to obey a simple power law as

$$\mu_{n,p}(T_l) = \mu_{n,p}(T_l = 300K)\cdot(300/T_l)^{\beta_{n,p}} \tag{12}$$

where the coefficients $\beta_{n,p}$ are determined from fittings with experiments. The temperature dependence of AlGaAs–GaAs refractive indices is assumed to be linear as given by $n_r(T_l) = n_r(T_l = 300K) + dn_r/dT_l \cdot (T_l - 300)$. The optical problem is recomputed using the updated refractive indices. Since the QW bandgap is carrier density dependent due to many-body effects, the k.p solver is also recomputed for the band-edge states [39]. With all the updated material parameters and optical-mode information, the electronic solver is then recomputed. This entire procedure repeats until full convergence is achieved.

## III. Simulation Results and Discussions

We simulate double-oxide-confined 980-nm VCSEL devices with varying oxide aperture sizes, and compare the simulation results with experimental measurements. The actual devices have square oxide apertures of varying aperture widths, $D =$ 3, 4.5, and 7$\mu$m. Since cylindrical geometry is assumed in

TABLE I
DEFAULT VALUES OF IMPORTANT SIMULATION PARAMETERS. NOTE THAT MOST OF THE PARAMETERS ARE IMPORTANT IN MORE THAN ONE MODEL DUE TO THE CLOSE INTERACTIONS BETWEEN THE THREE MODELS. THE PARAMETERS WITHOUT REFERENCES ARE FITTED VALUES

| | | |
|---|---|---|
| **Electronic Model Parameters** | | |
| $\tau_{n,p}$,QW | SRH lifetime in Eq.1 | $200ns$ ([36]) |
| $\tau_{n,p}$,SCH | SRH lifetime in Eq.1 | $10ns$ ([36]) |
| $\tau_{n,p}$,bulk(DBR) | SRH lifetime in Eq.1 | $0.3ns$ |
| $C_p$,QW | Auger coef. in Eq.2 | $0.1 \times 10^{-28} cm^6/s$ ([36],[40]) |
| $B_{spon}$,bulk(DBR)&SCH | spon. bimolecular recom. coef. | $1 \times 10^{-10} cm^3/s$ ([9]) |
| $\mu_n(300K)$,bulk(DBR) | elec. effective mobility in Eq.12 | $250 cm^2/Vs$ |
| $\mu_p(300K)$,bulk(DBR) | hole effective mobility in Eq.12 | $28 cm^2/Vs$ |
| $\lvert\vec{Q}_{max}\rvert$,QW | in Eq.10 | $1 \times 10^9/m$ ([28]) |
| $q_{z0}$,QW | in Eq.10 | $0.5 \times 10^9/m$ ([28]) |
| $\tau_{LO}$,QW | LO phonon lifetime in Eq.10 | $3ps$ ([20][23][30]) |
| **Optical Model/Photon Rate Equation Parameters** | | |
| $L_{mirror}$ | mirror loss | $3 \times 10^{11}/s$ |
| $n_{rl}$,DBR | DBR low refractive index | 3.00 ([52]) |
| $n_{rh}$,DBR | DBR high refractive index | 3.52 ([52]) |
| $k_n$,all | electron free carr. abs. coef. | $3 \times 10^{18} cm^2$ ([46]) |
| $k_p$,bulk(DBR)&SCH | hole free carr. abs. coef. | $7 \times 10^{18} cm^2$ ([46]) |
| $k_p$,QW | inter-valence band abs. coef. | $15 \times 10^{18} cm^2$ ([53]) |
| **Thermal Model Parameters** | | |
| $\kappa_{latt}$,bulk(DBR) | latt. thermal conductivity | $14 W/Km$ ([52]) |
| $\kappa_{latt}$,SCH | latt. thermal conductivity | $25 W/Km$ ([52]) |
| $\sigma_{thermal}$,contact | contact thermal resistance | $1.4 \times 10^{-7} m^2 K/W$ |
| $A_g$,QW | bandgap temp. coef. in Eq.11 | $-5.3 \times 10^{-4} eV/K$ ([52]) |
| $B_g$,QW | bandgap temp. coef. in Eq.11 | $231K$ ([52]) |
| $\beta_n$,all | in Eq.12 | 1 |
| $\beta_p$,all | in Eq.12 | 0.7 |
| $dn_r/dT$,all | temp. deriv. of refrac. index | $2.5 \times 10^{-4}$ ([12]) |

MINILASE, we use an aperture radius $R_a$ such that the aperture area matches, i.e., $\pi R_a^2 = D^2$. With this approximation, we simulate three devices with aperture radii equal to $R_a =$ 1.7, 2.5, and 4.0$\mu$m, correspondingly. The active region is composed of three 8-nm $In_{0.18}Ga_{0.82}As$ QWs, and the separate confinement heterojunction (SCH) regions are $Al_{0.1}Ga_{0.9}As$. The active cavity is of $1 - \lambda$ thickness. The oxide layers are placed adjacent to both the top and the bottom of the $1 - \lambda$ SCH cavity. The position of the oxide is intermediate: the central $0.15 - \lambda$ of the quarter-wavelength low index layer is oxidized. In the actual devices, the DBR pair is made up of $Al_{0.1}Ga_{0.9}As$–$Al_{0.9}Ga_{0.1}As$, and there are 22 pairs at the top and 35 pairs at the bottom. The refractive index profile corresponding exactly to this geometry is used for the optical simulations. In the electronic simulations, we use two bulk $Al_{0.2}Ga_{0.8}As$ regions to replace the DBR stacks, as discussed in Section II-A. The DBR regions are doped to $3 \times 10^{18}\text{cm}^{-3}$, and the remaining regions are unintentionally doped. The inner edge of the top annular contact is set to be 5.5 $\mu$m away from the oxide aperture edge, and the bottom contact covers the entire bottom surface.

We list the default values of parameters used in the simulation in Table I. The SRH recombination lifetimes and Auger coefficients can be determined by examining the electrical turn-on characteristics [36]. It was found that both the SRH and Auger recombinations are small at the turn-on condition for the 980-nm devices. The SRH lifetimes in the bulk (DBR) regions are significantly shorter due to high doping concentrations. For the free carrier and intervalence band absorptions, we use the typical bulk GaAs values, $3 \times 10^{-18}$ cm$^2$ for $k_n$ and $7 \times 10^{-18}$ cm$^2$ for $k_p$ [46] at the SCH and bulk regions. In the QWs, the intervalence band absorption can be significant, and a value of $15 \times 10^{-18}$ cm$^2$ is used for $k_p$. The values of the maximum LO phonon wave vectors in (10) are very important in computing the optical phonon temperature, because they directly determine the heat capacity of the optical phonons. It is possible to estimate these values from the width of the wave-vector spatial distribution of LO phonons, as noted in [28]. We use the same values here, as listed in Table I. Another important parameter is the effective energy relaxation time of the LO phonons, $\tau_{\text{LO}}$. A relatively wide range of values have been estimated for $\tau_{\text{LO}}$ in the literature, varying from 1 to 8 ps [20], [23], [30]. We use a default value of 3 ps in the simulation.

Based on the self-consistent model presented in Section II, the lattice temperature distribution is solved for the entire device. The lattice temperature contour is plotted in Fig. 4 for the 2.5-$\mu$m aperture device operating at 10 mA. It is evident that the temperature peak is in the central region of the active QW layers between the two oxide layers. From the gradients of the temperature profile, it can be seen that the generated thermal energy is removed through the top and bottom contacts. The thermal resistance used to model the electrical contacts (value listed in Table I) causes an approximate 5 K temperature rise above the ambient temperature (300 K) at the bias of 10 mA. It is observed that the oxide layers constrict the thermal diffusion of the heat due to the low thermal conductivity of the oxide. This situation becomes more severe for small aperture devices, and will deteriorate their high power performance.

The temperatures of the acoustic phonons, LO phonons, and carriers in the topmost QW are plotted in Fig. 5 for the same

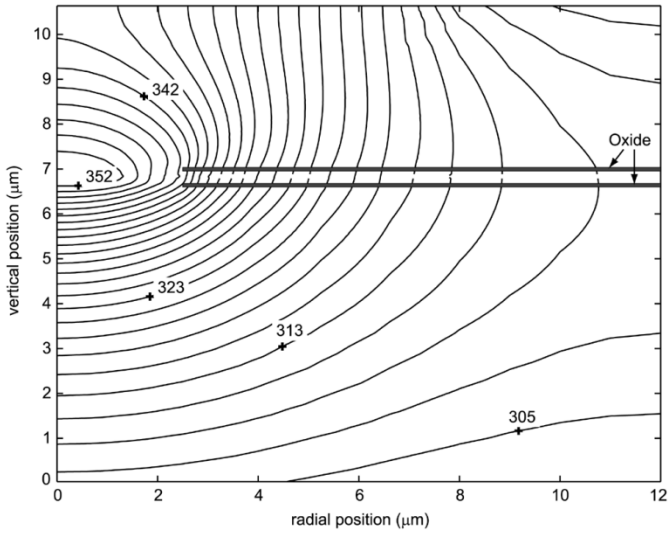


Fig. 4. Contour plot of simulated lattice temperature for the device with 2.5-$\mu$m aperture radius and operated at 10 mA.

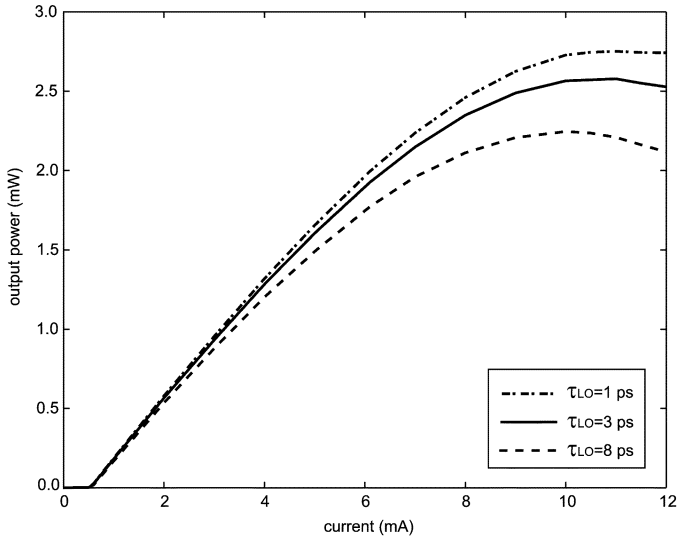


Fig. 6. Simulated light-current curves for the 2.5-$\mu$m aperture device with different LO phonon lifetime $\tau_{\rm ph}$.

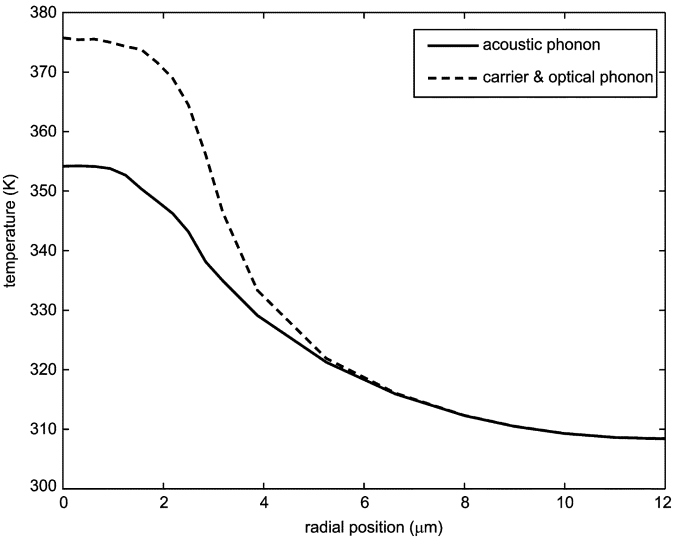


Fig. 5. Simulated carrier, LO phonon, and acoustic phonon temperature distributions along the topmost QW. The device oxide aperture radius is 2.5 $\mu$m and the current bias is 10 mA.

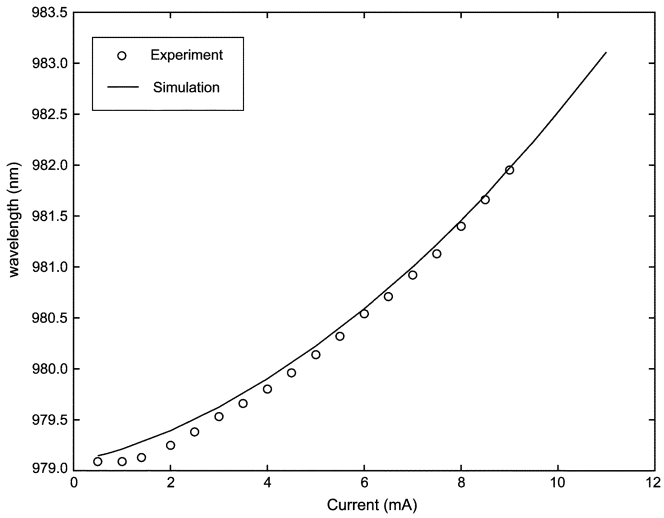


Fig. 7. Simulated and measured lasing wavelength plotted as a function of the current bias. The device aperture radius is 2.5 $\mu$m.

device and current bias as in Fig. 4. The difference between the carrier and LO phonon temperatures is very small due to rapid carrier-LO phonon scattering. It is clearly shown that they rise significantly above the acoustic phonon temperature. In this figure, a maximum difference of 20 K is observed in the central region. We note that the optical material gain is very sensitive to the carrier temperature. It is due to this same reason that the fast response of the carrier temperature can counteract the modulation of the carrier quasi-Fermi level and dampen the modulation response of laser diodes, as has been clarified in [38]. The gain spectrum is broadened at higher carrier temperature as determined by the Fermi–Dirac statistics. Therefore, the additional increase of the carrier temperature leads to more severe thermal rollover. This effect is demonstrated in Fig. 6, where the light-current curves are simulated for the 2.5-$\mu$m device with various $\tau_{\rm LO}$ values. A shorter LO phonon decay time lowers the additional rise of LO phonon and carrier temperatures, and hence leads to less severe thermal rollover. On the other hand, the output power saturates at a much lower level for large $\tau_{\rm LO}$ due to less efficient energy relaxation of the LO phonons.

Fig. 7 shows both experimental and simulated lasing wavelength as a function of the current bias for the 2.5-$\mu$m device. The red-shift of the wavelength with increasing bias is evident in the figure. Self-heating changes the temperature-dependent refractive indices of materials, and hence causes corresponding change of the resonant frequency of the lasing (fundamental) mode [50]. To model this effect, self-consistent coupling of the electronic, optical, and thermal solvers is necessary. As shown in Fig. 7, the agreement between experiment and simulation is very good; in this case we have used $dn_r/dT_l = 2.5 \times 10^{-4}$ in the simulation. The red-shift of the lasing wavelength is usually

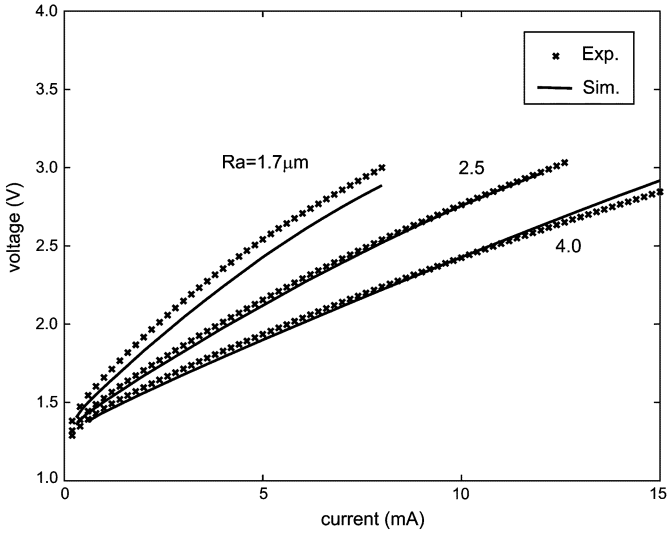


Fig. 8. Simulated and measured current-voltage characteristics for devices with aperture radii of 1.7, 2.5, and 4.0 $\mu$m.

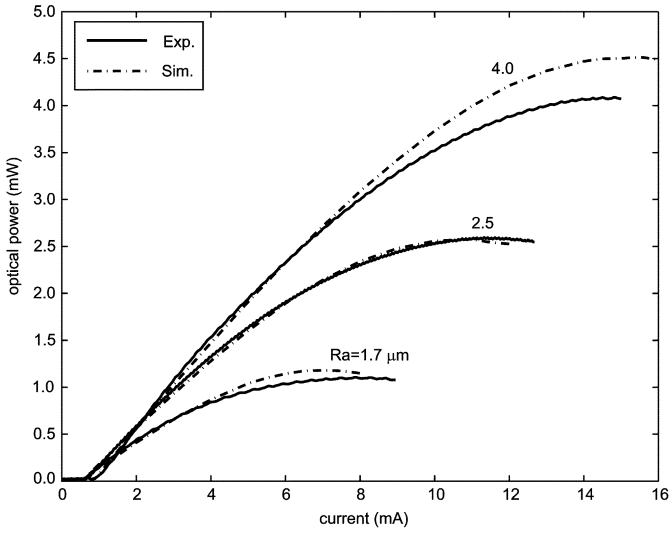


Fig. 9. Simulated and measure light-current characteristics for the same devices as in Fig. 8.

used as an indirect measurement of the internal lattice temperature rise caused by self-heating. It should be noted that the carrier temperature that is responsible for the optical gain reduction is actually significantly higher than the estimated temperature by this approach.

The measured and simulated $I$–$V$ curves are plotted in Fig. 8 for the three devices of varying oxide aperture sizes. The electrical characteristics are important in the modeling of the self-heating effects, because they determine the total electrical power injected into the device. The additional ohmic resistance above threshold in the figure is mostly caused by the DBR stacks. It can be seen that good matches with the experiments are obtained by simulating the DBR regions as bulk materials with effective mobilities. It is also shown that the series resistance responsible for the slope above the threshold increases with decreasing oxide aperture size. Since the same mobilities have been used in the simulations, it indicates that the difference is closely related to the device geometry. In general, smaller oxide aperture constricts the current flow more tightly, and thereby reduces the carrier conductance. It is interesting to note that the $I$–$V$ curves are not completely linear above threshold, and a decrease of the slope is actually observed at high bias. This observation is not due to the temperature dependence of the carrier mobilities, because they decrease at higher temperatures as determined by (12). It is also not completely due to the red-shift of the lasing wavelength, because the change in Fig. 7 corresponds to only a few millielectronvolts in terms of energy. The most likely cause is the reduction of the QW bandgap at elevated temperature according to (11), as briefly discussed in [51].

The measured and simulated $L$–$I$ curves are plotted in Fig. 9 for the three devices. As discussed in Section II-B, we have used a constant mirror loss of $3\times10^{11}$/s, and an additional scattering loss of $4.8, 2.5, 0.9\times10^{11}$/s for the aperture radii of 1.7, 2.5, and 4.0 $\mu$m, respectively, to match the threshold current and the initial slope efficiency. Excellent agreement is observed between experimental results and simulations for the thermal rollover behavior in the two smaller aperture devices. The discrepancy observed at high current bias for the 4.0-$\mu$m device is probably caused by multimode effects associated with the larger active area, which have not been accounted for in this work. There are three factors that are responsible for the observed aggravation of the thermal rollover in the smaller aperture devices: more tightly confined current injection and optical mode; larger DBR series resistance as shown in Fig. 8 and correspondingly increased Joule heating; and the blocking of the thermal fluxes by the oxides, as shown in Fig. 4.

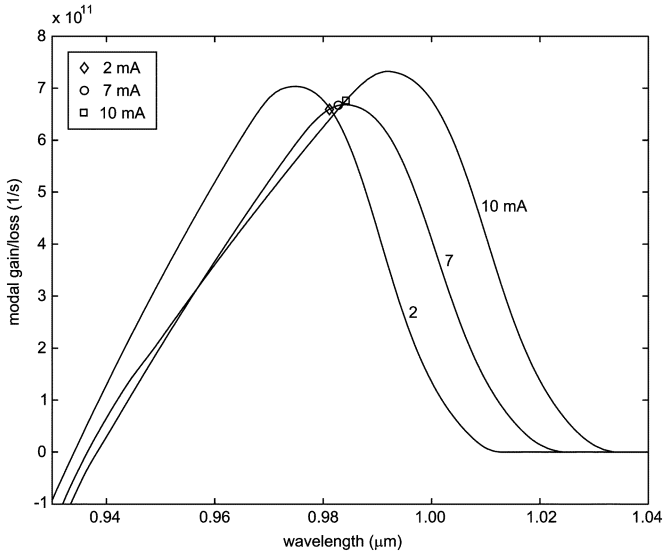


Fig. 10. Simulated modal gain spectrum and modal loss at the lasing frequency for a 2.5-$\mu$m aperture device at the current biases of 2, 7, and 10 mA.

The comprehensive device-level simulations enable deeper understandings of the underlying physics responsible for the thermal rollover behavior. Fig. 10 shows the simulated modal gain spectrums for the 2.5-$\mu$m device at three current biases. The optical losses are also shown at the corresponding lasing frequency. The slight red-shift of the lasing wavelength is in agreement with the results in Fig. 7. The small change of the optical loss at different biases is due to changes in the absorption

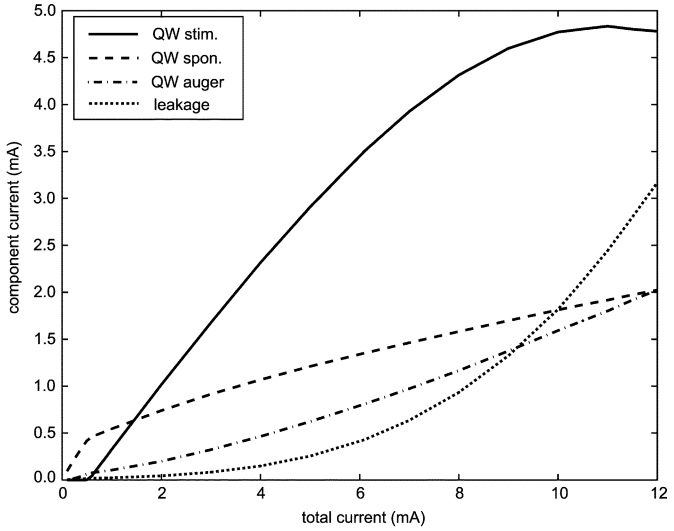


Fig. 11. Simulated current components as functions of the total current bias for a 2.5-$\mu$m aperture device.

loss $L_{\rm abs}$. When the current bias is increased, the rising carrier temperature leads to broadening of the gain spectrum, and the increasing lattice temperature causes QW bandgap shrinkage, as shown in Fig. 10. Both these effects lead to a reduction of the material gain at the resonant frequency at high injection level. The QW carrier density then has to increase correspondingly so that the modal gain at the resonant frequency is maintained equal to the loss under lasing condition. This results in an increase of the dark/leakage current and a further reduction of the power conversion efficiency. We must highlight that the $L$–$I$ curve of the 2.5-$\mu$m device rolls off at 7 mA in Fig. 9 despite the perfect gain peak alignment with the resonant frequency due to the favorable bandgap shift at the same bias in Fig. 10. This phenomenon can be accounted for by the reduction of the gain peak at elevated carrier temperatures. The overall effect demands a higher carrier density to maintain the gain at the loss level, resulting in the rolloff.

Different current components are plotted as functions of the total current bias for the 2.5-$\mu$m device in Fig. 11. The output power is proportional to the stimulated recombination current in the QWs. The QW leakage current eventually undergoes SRH and spontaneous recombination in the SCH and bulk (DBR) regions. It can be seen that the QW spontaneous recombination current is the dominant current component at threshold. It increases moderately with increasing current biases. The QW leakage current is insignificant below threshold, but increases rapidly at higher biases. It becomes the most significant channel responsible for the wastage of QW carriers and the decrease of the slope efficiency at the thermal rollover point. The SRH recombination included in this current component heats up the SCH and bulk regions. The QW Auger recombination current is small below threshold, but it becomes more significant at higher current biases due to its power law dependence on the carrier density. This process contributes to the heating of the QW carriers. In addition, the Joule heat elevates the lattice temperature, and the slow decay of the nonequilibrium LO phonons increases the QW carrier temperature. These two effects become stronger with increasing current biases.

## IV. Conclusion

We have developed a comprehensive numerical model to self-consistently simulate the coupled electronic, optical and thermal processes of oxide confined VCSELs. In this model, the electron and hole transport is modeled by Poisson and continuity equations with careful treatment of the boundaries at the quantum wells and the hetero-junctions. The optical properties are obtained based on an effective index method. A thermal diffusion equation is solved with proper boundary condition for acoustic phonon temperature distribution over the device. In addition, a carrier energy balance equation and an optical phonon rate equation are solved in the quantum wells to account for hot carriers and nonequilibrium optical phonon effects. Based on this comprehensive model, we have quantitatively simulated the self-heating and thermal rollover effects of VCSELs under CW operation. The hot carriers and nonequilibrium LO phonons are found to result in an additional carrier temperature rise and more severe thermal rollover. The simulation results have been carefully correlated with experimental measurements for VCSELs of varying oxide aperture sizes with respect to their optical, electrical and thermal characteristics. Excellent agreement between the simulations and experiments has been obtained. It has been shown that the thermal rollover becomes more severe for devices with small aperture sizes, mainly due to the increase of power density, DBR series resistance, and oxide thermal blocking. With the aid of detailed numerical simulations, the causes of the thermal rollover are explained as a positive feedback mechanism of the temperature increase and the reduction of the power conversion efficiency.

## Acknowledgment

The authors would like to thank D. Grasso for his assistance during the device measurements and Dr. C.-Z. Ning for useful discussions on the plasma heating effects. Y. Liu is very grateful to Prof. R. Dutton at Stanford University and the Interconnect Focus Center for their support.

## References

[1] G. Hasnain, K. Tai, L. Yang, Y. H. Wang, R. J. Fischer, J. D. Wynn, B. Weir, N. K. Dutta, and A. Y. Cho, "Performance of gain-guided surface-emitting lasers with semiconductor distributed bragg reflectors," *IEEE J. Quantum Electron.*, vol. 27, no. 6, pp. 1377–1385, Jun. 1991.

[2] D. L. Haffaker, D. G. Deppe, K. Kumar, and T. J. Rogers, "Native-oxide defined ring contact for low threshold vertical-cavity lasers," *Appl. Phys. Lett.*, vol. 65, pp. 97–99, 1994.

[3] K. D. Choquette, R. P. Schneider Jr., K. L. Lear, and K. M. Geib, "Low threshold voltage vertical-cavity lasers fabricated by selective oxidation," *Electron. Lett.*, vol. 30, pp. 2043–2044, 1994.

[4] K. L. Lear, A. Mar, K. D. Choquette, S. P. Kilcoyne, R. P. Schneider Jr., and K. M. Geib, "High-frequency modulation of oxide-confined vertical cavity surface emitting lasers," *Electron. Lett.*, vol. 32, pp. 457–458, 1996.

[5] K. D. Choquette, W. W. Chow, G. R. Hadley, H. Q. Hou, and K. M. Geib, "Scalability of small-aperture selectively oxidized vertical cavity lasers," *Appl. Phys. Lett.*, vol. 70, pp. 823–825, 1996.

[6] W. Nakwaski and M. Osinski, "Thermal properties of etched-well surface-emitting semiconductor lasers," *IEEE J. Quantum Electron.*, vol. 27, no. 6, pp. 1391–1401, Jun. 1991.

[7] ——, "Thermal properties of vertical cavity surface emitting semiconductor laser diodes," *Progr. Opt.*, vol. 38, pp. 165–262, 1998.

[8] J. W. Scott, R. S. Geels, S. W. Corzine, and L. A. Coldren, "Modeling temperature effects and spatial hole burning to optimize vertical-cavity surface-emitting laser performance," *IEEE J. Quantum Electron.*, vol. 29, pp. 1295–1308, 1993.

[9] S. F. Yu, W. N. Wong, P. Shum, and E. H. Li, "Theoretical analysis of modulation response and second-order harmonic distortion in vertical-cavity surface-emitting lasers," *IEEE J. Quantum Electron.*, vol. 32, no. 12, pp. 2139–2147, Dec. 1996.

[10] P. C. Chui and S. F. Yu, "Second-harmonic distortion in vertical-cavity surface-emitting lasers with lateral loss effects," *IEEE J. Select. Topics Quantum. Electron.*, vol. 5, no. 3, pp. 546–552, May–Jun. 1999.

[11] D. W. Winston and R. E. Hayes, "Optoelectronic device simulation of bragg reflectors and their influence on surface-emitting laser characteristics," *IEEE J. Quantum Electron.*, vol. 34, no. 4, pp. 707–715, Apr. 1998.

[12] J. Piprek, D. I. Babic, and J. E. Bowers, "Numerical analysis of 1.54 $\mu$m double-fused vertical-cavity lasers operating continuous-wave up to 33°C," *Appl. Phys. Lett.*, vol. 68, pp. 2630–2, 1996.

[13] J. Piprek, P. Abraham, and J. E. Bowers, "Self-consistent analysis of high-temperature effects on strained-layer multiquantum-well InGaAsP-InP lasers," *IEEE J. Quantum Electron.*, vol. 36, no. 3, pp. 366–374, Mar. 2000.

[14] J. Piprek, J. K. White, and A. J. SpringThorpe, "What limits the maximum output power of long-wavelength AlGaInAs–InP laser diodes?," *IEEE J. Quantum Electron.*, vol. 38, no. 9, pp. 1253–1259, Sep. 2002.

[15] M. Streiff, A. Witzig, M. Pfeiffer, P. Royo, and W. Fichtner, "A comprehensive VCSEL device simulator," *IEEE J. Sel. Topics Quantum. Electron.*, vol. 9, no. 3, pp. 879–891, May–Jun. 2003.

[16] G. R. Hadley, K. L. Lear, M. E. Warren, K. D. Choquette, J. W. Scott, and S. W. Corzine, "Comprehensive numerical modeling of vertical-cavity surface-emitting lasers," *IEEE J. Quantum Electron.*, vol. 32, no. 4, pp. 607–616, Apr. 1996.

[17] B. Etienne, J. Shah, R. F. Leheny, and R. E. Nahory, "Influence of hot carriers on the temperature dependence of threshold in 1.3-$\mu$m InGaAsP lasers," *Appl. Phys. Lett.*, vol. 41, pp. 1018–1020, 1982.

[18] W. Potz and P. Kocevar, "Electronic power transfer in pulsed laser excitation of polar semiconductors," *Phys. Rev. B*, vol. 28, pp. 7040–7047, 1983.

[19] W. Potz, "Hot-phonon effects in bulk GaAs," *Phys. Rev. B*, vol. 36, pp. 5016–5019, 1987.

[20] J. A. Kash, S. S. Jha, and J. C. Tsang, "Picosecond Raman studies of the Frolich interaction in semiconductor alloys," *Phys. Rev. Lett.*, vol. 58, pp. 1869–1872, 1987.

[21] M. Kesler, C. S. Harder, and E. E. Latta, "Carrier heating in AlGaAs single quantum well laser diodes," *Appl. Phys. Lett.*, vol. 59, pp. 2775–2777, 1991.

[22] M. Nido and A. Suzuki, "Observation of carrier heating in a 1.5 $\mu$m band multiquantum-well semiconductor laser amplifier by time-resolved measurement for amplified spontaneous emission spectrum," *Appl. Phys. Lett.*, vol. 64, pp. 681–683, 1993.

[23] S. Usher and G. P. Srivastava, "Theoretical study of the anharmonic decay of nonequilibrium LO phonons in semiconductor structures," *Phys. Rev. B*, vol. 50, pp. 14 179–14 186, 1994.

[24] C. Y. Tsai, L. F. Eastman, and Y. H. Lo, "Hot carrier and hot phonon effects on high-speed quantum well lasers," *Appl. Phys. Lett.*, vol. 63, pp. 3408–3410, 1993.

[25] T. Rossler, R. A. Indik, G. K. Harkness, J. V. Moloney, and C. Z. Ning, "Modeling the interplay of thermal effects and transverse mode behavior in native-oxide-confined vertical-cavity surface-emitting lasers," *Phys. Rev. A*, vol. 58, pp. 3279–3292, 1998.

[26] V. B. Gorfinkel and S. Luryi, "High-frequency modulation and suppression of chirp in semiconductor lasers," *Appl. Phys. Lett.*, vol. 62, pp. 2923–2925, 1993.

[27] C.-Y. Tsai, C.-Y. Tsai, R. M. Spencer, Y.-H. Lo, and L. F. Eastman, "Nonlinear gain coefficients in semiconductor lasers: Effects of carrier heating," *IEEE J. Quantum Electron.*, vol. 32, no. 2, pp. 201–212, Feb. 1996.

[28] M. Grupen and K. Hess, "Simulation of carrier transport and nonlinearities in quantum-well laser diodes," *IEEE J. Quantum Electron.*, vol. 34, no. 1, pp. 120–140, Jan. 1998.

[29] S. F. Yu, "Dynamic behavior of vertical-cavity surface-emitting lasers," *IEEE J. Quantum Electron.*, vol. 32, no. 7, pp. 1168–1179, Jul. 1996.

[30] M. Nido and A. Suzuki, "Slow carrier-phonon interaction in InGaAs-InGaAsP multiquantum well investigated by time-development of carrier temperature and gain," *IEEE J. Sel. Topics Quantum. Electron.*, vol. 1, no. 2, pp. 308–315, Jun. 1995.

[31] C. Z. Ning and J. V. Moloney, "Plasma-heating induced intensity-dependent gain in semiconductor lasers," *Appl. Phys. Lett.*, vol. 66, pp. 559–561, 1994.

[32] C. Z. Ning, R. A. Indik, J. V. Moloney, and S. W. Koch, "Effects of plasma and lattice heating in VCSELs," in *Proc. SPIE, Physics and Simulation of Optoelectronic Devices III*, vol. 2399, M. Osinski and W. W. Chow, Eds., 1995, pp. 617–628.

[33] F. A. Oyafuso, B. D. Klein, L. F. Register, and K. Hess, "Fully coupled electrical and optical simulation of VCSELs," in *Proc. SPIE, Vertical-Cavity Surface-Emitting Lasers IV*, vol. 3946, K. D. Choquette and C. Lei, Eds., 2000, pp. 108–116.

[34] Y. Liu, W.-C. Ng, F. Oyafuso, B. Klein, and K. Hess, "Simulating the modulation response of VCSELs: The effects of diffusion capacitance and spatial hole-burning," *Proc. IEE Optoelectronics*, vol. 149, pp. 182–188, 2002.

[35] Y. Liu, W.-C. Ng, B. Klein, and K. Hess, "Effects of the spatial nonuniformity of optical transverse modes on the modulation response of vertical-cavity surface-emitting lasers," *IEEE J. Quantum Electron.*, vol. 39, no. 1, pp. 99–108, Jan. 2003.

[36] Y. Liu, K. D. Choquette, and K. Hess, "The electrical turn-on characteristics of vertical-cavity surface-emitting lasers," *Appl. Phys. Lett.*, vol. 83, pp. 4104–4106, 2003.

[37] W.-C. Ng, "Thermal and optical simulations of vertical cavity surface emitting lasers," Ph.D. dissertation, Dept. Elect. Comput. Eng., Univ. Illinois at Urbana-Champaign, Nov. 2002.

[38] K. Hess, *Advanced Theory of Semiconductor Devices*. Piscataway, NJ: IEEE Press, 2000.

[39] F. Oyafuso, P. von Allmen, M. Grupen, and K. Hess, "Inclusion of band-structure and many-body effects in a quantum well laser simulator," *VLSI Des.*, vol. 8, pp. 463–468, 1998.

[40] L. A. Coldren and S. W. Corzine, *Diode Lasers and Photonic Integrated Circuits*. New York: Wiley, 1995.

[41] P. Bienstman, R. Baets, J. Vukusic, A. Larsson, M. J. Noble, M. Brunner, K. Gulden, P. Debernardi, L. Fratta, G. P. Bava, H. Wenzel, B. Klein, O. Conradi, R. Pregla, S. A. Riyopoulos, J.-F. P. Seurin, and S. L. Chuang, "Comparison of optical VCSEL models on the simulation of oxide-confined devices," *IEEE J. Quantum Electron.*, vol. 37, no. 12, pp. 1618–1631, Dec. 2001.

[42] W.-C. Ng, Y. Liu, and K. Hess, "Resonant-wavelength control and optical-confinement analysis for graded SCH VCSELs using a self-consistent effective-index method," *J. Lightwave Technol.*, vol. 21, no. 2, pp. 555–560, Feb. 2003.

[43] E. R. Hegblom, D. I. Babic, B. J. Thibeault, and L. A. Coldren, "Scattering losses from dielectric apertures in vertical-cavity lasers," *IEEE J. Sel. Topics Quantum. Electron.*, vol. 3, no. 2, pp. 379–389, Apr. 1997.

[44] H. Yi, J. Diaz, B. Lane, and M. Razeghi, "Optical losses of Al-free lasers for $\lambda = 0.808$ and $0.98\,\mu$m," *Appl. Phys. Lett.*, vol. 69, pp. 2983–2985, 1996.

[45] G. H. B. Thompson, P. A. Kirkby, and J. E. A. Whiteaway, "The analysis of optical scattering in double-heterostructure and five-layer heterostructure (GaAl)As/GaAs injection lasers," *IEEE J. Quantum Electron.*, vol. QE-11, no. 7, pp. 481–488, Jul. 1975.

[46] H. C. Casey and M. B. Panish, *Heterostructure Lasers*. New York: Academic, 1978.

[47] M. Asada, A. R. Adams, K. E. Stubkjaer, Y. Suematsu, Y. Itaya, and S. Arai, "The temperature dependence of the threshold current of GaInAsP–InP DH lasers," *IEEE J. Quantum Electron.*, vol. QE-17, no. 5, pp. 611–619, May 1981.

[48] L. Rota, M. Grupen, and K. Hess, "Spectral hole burning and carrier-carrier interaction in semiconductor quantum well lasers: A Monte Carlo investigation," in *Hot Carriers in Semiconductors*, K. Hess, J. P. Leburton, and U. Ravaioli, Eds. New York: Plenum, 1996.

[49] R. Stratton, "Diffusion of hot and cold electrons in semiconductor barriers," *Phys. Rev.*, vol. 126, pp. 2002–2014, 1962.

[50] M. Brunner, K. Gulden, R. Hovel, M. Moser, and M. Ilegems, "Thermal lensing effects in small oxide confined vertical-cavity surface-emitting lasers," *Appl. Phys. Lett.*, vol. 76, pp. 7–9, 2000.

[51] M. Fukuda, *Optical Semiconductor Devices*. New York: Wiley, 1998.

[52] S. Adachi, "Optical Properties of AlGaAs: Transparent and interband-transition regions (tables)," in *Properties of Aluminum Gallium Arsenide*, S. Adachi, Ed. Stevenage, U.K.: IEE Press, 1993.

[53] C. H. Henry, R. A. Logan, F. R. Merritt, and J. P. Luongo, "The effect of intervalence band absorption on the thermal behavior of InGaAsP lasers," *IEEE J. Quantum Electron.*, vol. QE-19, no. 6, pp. 947–952, Jun. 1983.

[54] S. Adachi, "Thermal Conductivity of AlGaAs," in *Properties of Aluminum Gallium Arsenide*, S. Adachi, Ed. Stevenage, U.K.: IEE Press, 1993.

[55] F. H. Pollak, "Temperature effects on the energy band parameters of AlGaAs," in *Properties of Aluminum Gallium Arsenide*, S. Adachi, Ed. New York: IEE Press, 1993.

**Yang Liu** (M'03) received the B.S. degree in physics from the University of Science and Technology of China, Hefei, China, in 1998 and the Ph.D. degree in physics from the University of Illinois at Urbana-Champaign in 2002.

In 2003, he joined the Integrated Circuit Laboratory, Stanford University, Stanford, CA, as a Research Associate. His major research interests are the physics and simulations of semiconductor devices, including transistors, LEDs, VCSELs, and mode-locked lasers and their impact on integrated circuits and systems.

**Wei-Choon Ng** (S'98–M'03) received the B.Eng. (with first class honors) and M.Eng. degrees in electrical engineering from the National University of Singapore, Singapore, in 1996 and 1998, respectively, and the Ph.D. degree in electrical engineering from the University of Illinois at Urbana-Champaign in 2002.

In 1995, he worked on optical thin-film coating in British Telecoms Labs, Ipswich, U.K., for his industrial placement. He was a Graduate Research Assistant with the Computational Electronics Group, University of Illinois at Urbana-Champaign from 1999 to 2002. He is currently an Optoelectronics Development Engineer with Integrated Systems Engineering, San Jose, CA. His research interests mainly focus on semiconductor transport, thermal modeling of semiconductor lasers, modeling LEDs, modeling guided-wave devices, device simulation, and computational electromagnetics.

Dr. Ng is a member of the IEEE Electron Devices Society and a Senior Research Fellow of the International Society for Philosophical Enquiry (ISPE).

**Kent D. Choquette** (M'97–F'03) received the B.S. degrees in engineering physics and applied mathematics from the University of Colorado at Boulder in 1984 and the M.S. and Ph.D. degrees in materials science from the University of Wisconsin at Madison in 1985 and 1990, respectively.

From 1990 to 1992, he held a postdoctoral appointment at AT&T Bell Laboratories, Murray Hill, NJ. In 1993, he joined Sandia National Laboratories, Albuquerque, NM. He became a Professor in the Electrical and Computer Engineering Department of the University of Illinois at Urbana-Champaign in 2000. His research centers around the design, fabrication and characterization of vertical-cavity surface emitting lasers (VCSELs), photonic crystals, and other optoelectronic devices. His research interests include novel fabrication technologies, hybrid integration techniques, and nano-fabrication processes. He has authored over 100 publications and 3 book chapters, and has presented numerous invited talks and tutorials on VCSELs.

Dr. Choquette is an Associate Editor of the IEEE PHOTONIC TECHNOLOGY LETTERS, and as served previously as an Associate Editor for the JOURNAL OF QUANTUM ELECTRONICS and as a Guest Editor for the IEEE JOURNAL OF SELECTED TOPICS IN QUANTUM ELECTRONICS, and was previously an IEEE Lasers and Electro-Optics Society (LEOS) Distinguished Lecturer during 2000–2002. He is a Fellow of LEOS and a member of the Optical Society of America (OSA).

**Karl Hess** (M'79–SM'83–F'85) received the Ph.D. degree in applied physics from the University of Vienna, Vienna, Austria, in 1970.

Currently, he holds the Swanlund Endowed Chair and is Professor of Electrical and Computer Engineering and Professor of Physics at the University of Illinois at Urbana-Champaign. He is also with the Beckman Institute, where his current research is in the area of molecular and electronic nanostructures. He has dedicated the major portion of his research to electronic transport in semiconductors and semiconductor devices, with particular emphasis on hot electron effects and effects pertinent to device miniaturization. He is particularly interested in problems that require large computational resources for their solution.

Dr. Hess has received numerous awards, including the IEEE J. J. Ebers Award of the IEEE Electron Devices Society in 1993 and the IEEE Sarnoff Field Award for Electronics in 1995. He is a Fellow of the American Physics Society, the American Association for the Advancement of Science, and the American Academy of Arts and Sciences, and a member of the National Academy of Engineering and the National Academy of Sciences.